

Comparative Study on Charge Radii and Their Kinks at Magic Numbers

Tomoya Naito^{a,b}, Tomohiro Oishi^c, Hiroyuki Sagawa^{d,e}, Zhiheng Wang^{f,g}

^aRIKEN Interdisciplinary Theoretical and Mathematical Sciences (iTHEMS), Wako, 351-0198, Japan

^bDepartment of Physics, Graduate School of Science, The University of Tokyo, Tokyo 113-0033, Japan

^cYukawa Institute for Theoretical Physics, Kyoto University, Kyoto 606-8502, Japan

^dCenter for Mathematics and Physics, University of Aizu, Aizu-Wakamatsu 965-8560, Japan

^eRIKEN Nishina Center, Wako 351-0198, Japan

^fSchool of Nuclear Science and Technology, Lanzhou University, Lanzhou 730000, China

^gFrontiers Science Center for Rare Isotopes, Lanzhou University, Lanzhou 730000, China

Abstract

Isotope dependence of charge radii, i.e., isotope shifts, obtained by the Skyrme Hartree-Fock, the relativistic mean-field, and the relativistic Hartree-Fock calculations are compared. The tensor interaction plays a crucial role to reproduce the “kink” behaviour, irregularity of isotope shifts at the neutron magic number; thus in the non-relativistic calculation, the “kink” behaviour at neutron magic numbers is reproduced well if the spin-orbit interaction is considered properly, where the isoscalar strength of the spin-orbit interaction and the isovector one need not be different. The symmetry energy is also important to reproduce the kink.

Keywords: Charge radius; Skyrme Hartree-Fock calculation; Relativistic mean-field calculation; Relativistic Hartree-Fock calculation

1. Introduction

Charge radii of atomic nuclei R_{ch} are one of the important properties of atomic nuclei, which can be measured precisely via the electron scattering [1, 2] and the laser spectroscopy [3, 4]. The isotope dependence of R_{ch} , i.e., the isotope shift, has been discussed for a long time theoretically and experimentally. The slope of R_{ch} as a function of the neutron number N is known to change at the neutron magic number, which is called the “kink” behaviour. It was discussed in Ref. [5] that the kink behaviour of Pb isotopes can be reproduced if the strengths of isoscalar and isovector spin-orbit interaction in the Skyrme energy density functional (EDF) is different. Recently, it was discussed using the M3Y-P6a interaction that the kink behaviour may occur due to the three-body spin-orbit interaction [6]. This behaviour was also discussed in Ref. [7], in which the relativistic mean-field calculation was used, that the occupation probability above the shell gap may be important.

In this paper, we compare R_{ch} of Sn and Pb isotopes obtained by the non-relativistic Skyrme Hartree-Fock (SHF) [8], the relativistic mean-field (RMF) [9, 10], and the relativistic Hartree-Fock (RHF) [11] calculations. This comparison enables us to discuss the kink behaviour from two perspectives on the spin-orbit splitting. In the non-relativistic Skyrme energy-density functional calculation, the spin-orbit splitting is phenomenologically determined by the corresponding parameters, the isoscalar spin-orbit strength W_0 and the isovector one W'_0 . On the other side, in the relativistic mean-field calculations, where the single-particle state is described with the Dirac equation obtained self-consistently from the relativistic EDF, the tensor interaction can also be included naturally when the Fock terms are explicitly considered. Using such comparison, we

will find that the tensor interaction, and its outcome, which is spin-orbit mean field, is important to reproduce the kink behaviour. In addition, we will show that the symmetry energy of the nuclear equation of state also affects the kink behaviour.

2. Theoretical Framework

In the SHF calculation, the following Skyrme EDFs are used: SAMi [12], SGII [13], SLy4 [14], SLy5 [14], SkM* [15], HFB9 [16], UNEDF0 [17], UNEDF1 [18], and UNEDF2 [19]. In addition, the Skyrme EDF with the tensor interaction “SAMi-T” [20] is used, in which all the parameters, including the tensor interaction, are fitted altogether. To see the effect of the tensor interaction, the SAMi-T EDF without the tensor interaction is also used, which will be referred to as “SAMi-noT”. In order to see whether properties of nuclear equation of state (EoS) affect the behaviour, the SAMi EDF but the different assumption for the effective mass, the symmetry energy, and the nuclear incompressibility, called “SAMi-m” [21], “SAMi-J” [21], and “SAMi-K” [22] families are also tested. The pairing interaction is considered by using the Hartree-Fock-Bogoliubov calculation with the volume type pairing interaction [23], whose strengths are determined to reproduce the neutron pair gap of ^{120}Sn as $\Delta_n = 1.4$ MeV. The strengths are shown in the supplemental material. All the calculations are performed by using the harmonic oscillator basis [24] and all the results are spherically symmetric.

In the relativistic framework, there are two procedures: the RMF and RHF calculations. In the RMF calculation, one drops the Fock term and correspondingly the EDF is optimized in order to reproduce the reference data. The RHF calculation,

on the other hand, takes the Fock term into account and the parameters of the relativistic EDF are consistently optimized. In the RMF calculation, the DD-PC1 [25], DD-ME2 [26], PKDD [27], and DD-LZ1 [28] EDFs are used, while in the RHF calculation, the PKO1 [29], PKO2 [29], PKO3 [29], PKA1 [30], and the modified version of the PKO1, which will be referred to as the PKO1* [31], are used. The pairing correlation is considered by using the Bardeen-Cooper-Schrieffer (BCS) theory; the Tian-Ma-Ring (TMR) type pairing interaction [32] is used for DD-PC1 and DD-ME2 and the surface type pairing interaction [33] with the pairing strength of $V_0 = -500 \text{ MeV} \cdot \text{fm}^3$ is used for DD-ME2, PKDD, DD-LZ1, PKO1, PKO2, PKO3, PKO1*, and PKA1. All the calculations are performed with assuming the spherical symmetry by using the harmonic oscillator or Woods-Saxon basis.

In this paper, the same pairing strengths are used for both the proton-proton channel and the neutron-neutron one.

After the proton and neutron root-mean-square radii, R_p and R_n , are obtained by using SHF, RMF, and RHF, the charge radius R_{ch} is calculated by

$$R_{\text{ch}}^2 = R_p^2 + r_{E_p}^2 + \frac{N}{Z} r_{E_n}^2 + \langle r^2 \rangle_{\text{SO}_p} + \frac{N}{Z} \langle r^2 \rangle_{\text{SO}_n}, \quad (1)$$

where $r_{E_p} = 0.8409 \text{ fm}$ is the single proton radius and $r_{E_n}^2 = -0.1161 \text{ fm}^2$ is the single neutron mean-square radius [34]. The spin-orbit contributions $\langle r^2 \rangle_{\text{SO}_p}$ and $\langle r^2 \rangle_{\text{SO}_n}$ obtained in Ref. [35] are calculated with the nucleon magnetic moments $\kappa_p = 1.793$ and $\kappa_n = -1.913$ [34].

3. Calculation Results

3.1. Systematic Behaviour

First of all, the mass number A dependence of $R_{\text{ch}}(^A\text{Sn}) - R_{\text{ch}}(^{132}\text{Sn})$ calculated by using the non-relativistic (SHF) and the relativistic (RMF and RHF) schemes are shown in Figs. 1(a) and 2(a), respectively. For comparison, experimental data [3, 36] are also plotted. In order to see the behaviour efficiently, the relative change of charge radii $\Delta R_{\text{ch}}^Z(A) = R_{\text{ch}}^Z(A) - R_{\text{ch}}^Z(A-2)$ are plotted in the panels (b). Figures for Ca and Pb isotopes are shown in the supplemental material.

It can be seen that most EDFs reproduce the A dependence of R_{ch} of stable nuclei ($62 \leq N \leq 74$) appreciably except UNEDF2, PKA1, and DD-LZ1. Most EDFs reproduce those for Pb isotopes appreciably. In contrast, for Ca isotopes, as seen in Figs. B.1 and B.2 in supplemental materials, no EDF reproduces the A dependence for Ca isotopes, which is a widely-known problem. For this staggering behaviour of R_{ch} in Ca isotopes, there has been one possible solution by using the Fayans EDF, instead of Skyrme one [37, 38, 39]. However, the Fayans calculation goes beyond the scope of this work.

Here, we focus only on the kink behaviour. To discuss the size of kink quantitatively, we define the size of kink $\Delta^2 R_{\text{ch}}^Z$ as

$$\begin{aligned} \Delta^2 R_{\text{ch}}^Z &= \Delta R_{\text{ch}}^Z(A_{\text{magic}} + 2) - \Delta R_{\text{ch}}^Z(A_{\text{magic}}) \\ &= R_{\text{ch}}^Z(A_{\text{magic}} + 2) - 2R_{\text{ch}}^Z(A_{\text{magic}}) + R_{\text{ch}}^Z(A_{\text{magic}} - 2), \end{aligned} \quad (2)$$

Table 1: Kink size of Sn, $\Delta^2 R_{\text{ch}}^{\text{Sn}}$, calculated by using non-relativistic EDF together with $\Delta R_{\text{ch}}^{\text{Sn}}(132)$ and $\Delta R_{\text{ch}}^{\text{Sn}}(134)$ shown in fm.

EDF	$\Delta R_{\text{ch}}^{\text{Sn}}(132)$	$\Delta R_{\text{ch}}^{\text{Sn}}(134)$	$\Delta^2 R_{\text{ch}}^{\text{Sn}}$
UNEDF1	+0.014913	+0.011886	-0.003559
UNEDF0	+0.012495	+0.010479	-0.002632
UNEDF2	+0.014850	+0.012571	-0.002315
SkM*	+0.011456	+0.011027	-0.000522
HFB9	+0.011302	+0.012222	+0.000318
SLy5	+0.010568	+0.012363	+0.001060
SLy4	+0.010665	+0.012449	+0.001139
SGII	+0.011436	+0.013446	+0.001257
SAMi-noT	+0.011102	+0.017312	+0.004194
SAMi-T	+0.011196	+0.018507	+0.004879
SAMi	+0.011229	+0.021092	+0.006717
Expt.	+0.0074	+0.0224	+0.015000

Table 2: Same as Table 1 but by using relativistic EDF.

EDF	$\Delta R_{\text{ch}}^{\text{Sn}}(132)$	$\Delta R_{\text{ch}}^{\text{Sn}}(134)$	$\Delta^2 R_{\text{ch}}^{\text{Sn}}$
PKDD	+0.011088	+0.014166	+0.002014
DD-PC1	+0.011411	+0.015862	+0.003102
DD-ME2 (Surface)	+0.009055	+0.015159	+0.005059
DD-ME2 (TMR)	+0.009290	+0.015587	+0.005161
PKO2	+0.011424	+0.018474	+0.005993
PKO1	+0.010172	+0.019566	+0.007757
PKA1	+0.005691	+0.016512	+0.010145
DD-LZ1	+0.004836	+0.016631	+0.010959
PKO3	+0.009455	+0.023896	+0.012728
PKO1*	+0.009629	+0.025748	+0.013731
Expt.	+0.0074	+0.0224	+0.015000

where A_{magic} is the mass number corresponding to doubly-magic nuclei, i.e., $A_{\text{magic}} = 48$ for $Z = 20$ (Ca), $A_{\text{magic}} = 132$ for $Z = 50$ (Sn), and $A_{\text{magic}} = 208$ for $Z = 82$ (Pb). This corresponds to the discretized second derivative of R_{ch} at $A = A_{\text{magic}}$, which is related to the curvature of the graph in the continuum limit. The larger value corresponds to the larger (stronger) kink. The kink sizes for Sn isotopes are summarized in Tables 1 and 2. These tables are sorted by $\Delta^2 R_{\text{ch}}^{\text{Sn}}$. Tables for Ca and Pb isotopes are shown in the supplemental material. From Tables 1, 2, B.2, B.3 B.4, and B.5, one general tendency is found: The relativistic (RMF and RHF) calculations give stronger kinks than the non-relativistic (SHF) ones, even depending on which EDF is employed. In the non-relativistic SHF, UNEDF series somehow yields a smaller kink commonly for Ca, Sn, and Pb isotopes. In the relativistic results for the Ca and Sn isotopes, the RHF calculations give larger kinks than those from the RMF ones, except the DD-LZ1 EDF. Also, in the case of Pb given in Table B.5, there is not a well-ordered tendency between our RMF and RHF results.

The kink at $A = 132$ can be discussed easily by the panels (b); the value of ΔR_{ch} increases suddenly at $A = 134$ if the kink, i.e., sudden increase of the slope of R_{ch} as a function of A , appears at $A = 132$. One can easily find that the SHF calculations except SAMi, SAMi-noT, and SAMi-T provide the smaller kink

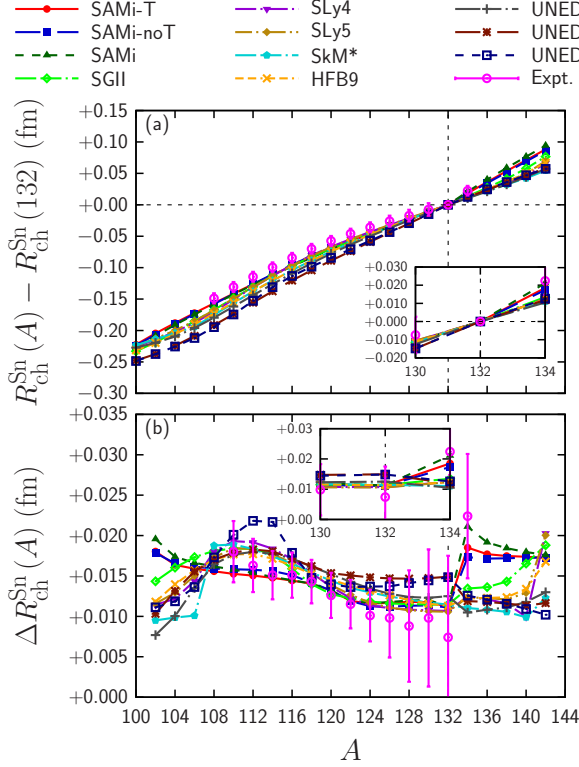


Figure 1: (a) Charge radii for Sn isotope, $R_{\text{ch}}(A) - R_{\text{ch}}(132\text{Sn})$, as functions of A calculated by using non-relativistic EDFs. For comparison, experimental data [3, 36] are also plotted. (b) Relative change of charge radii ΔR_{ch} as functions of A . For more detail, see the text.

than the relativistic (RMF and RHF) ones. In general, the RHF calculations provide the larger kink than the RMF ones. This can be understood as follows: As will be discussed, the spin-orbit interaction is important for the kink behaviour [6]. The spin-orbit mean field appears from both the Dirac operator itself and the tensor interaction in RHF calculation, while only from the Dirac operator in RMF calculation; hence, the spin-orbit interaction of the RMF calculation is not complete compared to that of the RHF calculation. The spin-orbit interaction in the Skyrme calculation is introduced by hand as the W_0 and W'_0 terms without any density dependence, and the Schrödinger operator does not introduce the spin-orbit interaction; hence, the spin-orbit interaction cannot be perfect.

Among Skyrme EDFs, the UNEDF series provide the “anti-kink”; the SkM* and HFB9 do not provide visible kink; and the SLy4, SLy5, and SGI give the kink. The SAMi, SAMi-noT, and SAMi-T provide the kink larger than the other Skyrme EDF. The SAMi EDF is constructed to give the better description of spin-isospin properties, such as Gamow-Teller resonances [12], where its strength stems from the spin-isospin transitions involving the spin-orbit partner levels. Hence, we conjecture that the modeling with respect to the spin-orbit splitting is essential to describe the kink better. Note that the SGI is also constructed towards Gamow-Teller resonances [13] but it does not give the kink as large as the SAMi. It is worthwhile to men-

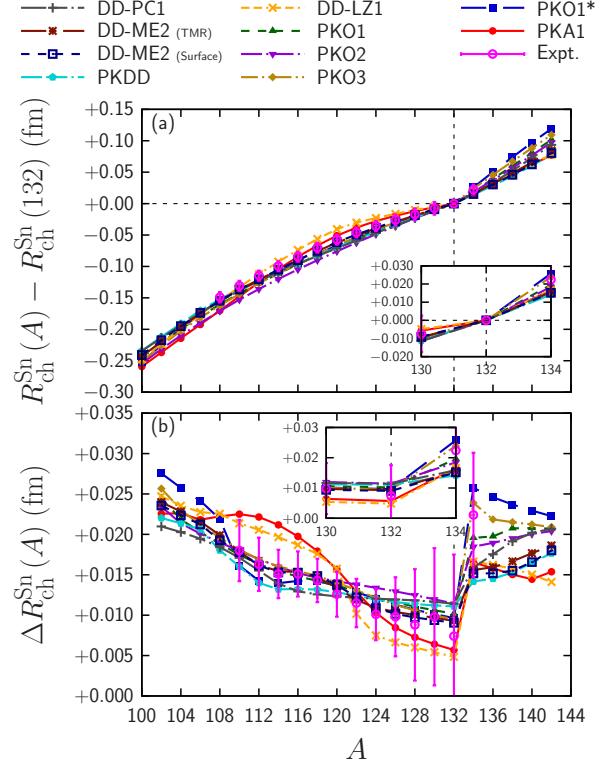


Figure 2: Same as Fig. 1 but by using relativistic EDFs.

tion that, in Pb isotopes, SAMi series and SGI give stronger kinks than other Skyrme EDFs.

The SkI4 EDF also gives the kink behaviour of Pb isotopes [5]. Reference [5] claims that the strengths of the isoscalar and isovector spin-orbit interactions, W_0 and W'_0 , which are identical in the normal Skyrme EDFs, are important. In the SGI EDF, the two strengths are identical, $W_0 = W'_0$; in the SkI4 EDF, the isoscalar and isovector spin-orbit interactions have opposite signs, namely, $W'_0 < 0 < W_0$ and $|W'_0| < W_0$; in the SAMi EDF, the isoscalar and isovector spin-orbit interactions are the same direction, but the strengths are different, $0 < W'_0 < W_0$. Since their settings of W_0 and W'_0 have no correspondence, there is not a clear outcome on which combination

Table 3: Mesons considered in PKDD, DD-ME2, DD-LZ1, PKO1, PKO2, PKO3, PKO1*, and PKA1 EDFs. All the couplings are density dependent.

EDF	π -PV	ρ -V	ρ -T	ρ -VT	ω -V	σ -S
PKDD	No	Yes	No	No	Yes	Yes
DD-ME2	No	Yes	No	No	Yes	Yes
DD-LZ1	No	Yes	No	No	Yes	Yes
PKA1	Yes	Yes	Yes	Yes	Yes	Yes
PKO1	Yes	Yes	No	No	Yes	Yes
PKO2	No	Yes	No	No	Yes	Yes
PKO3	Yes	Yes	No	No	Yes	Yes
PKO1*	Yes	Yes	No	No	Yes	Yes

of W_0 and W'_0 values are the best for the kink behaviour.

Comparing the results of the SAMi-T and the SAMi-noT EDFs, one can see how the Skyrme tensor interaction affect the kink behaviour. Although the SAMi-T EDF gives the stronger kink than the SAMi-noT EDF and, especially, the Skyrme tensor interaction makes the slope above the shell gap steeper, its effect is not so significant. Moreover, the shell structure, which will be discussed later, is not changed much. Therefore, the Skyrme tensor interaction introduces the spin-orbit mean field but its effect to ground-state properties may not be strong. This may be because the effect of the tensor interaction may be already included in the original spin-orbit interaction during the fitting procedure.

Next, we shall focus on the relativistic calculation. Except the DD-LZ1 EDF, the RMF calculations give the smaller kink than the RHF calculation, while the DD-LZ1 EDF gives the comparable size of kink with the RHF calculations. Comparing two calculation of DD-ME2, one can easily find that these two pairing interactions give almost the same kink size. Among the RHF calculation, the kink size of PKO2 is weakest and PKO3 and PKO1* give the appreciable kink size. It should be noted that although the PKA1 and the DD-LZ1 give the strong kink, their slopes above $N = 82$ are not so steep; the reason why their kink sizes are large is that the slopes below $N = 82$ are loose. Indeed, the slope above $N = 82$ of the PKA1 is the smallest among the RHF calculations, while the slope above $N = 82$ of the DD-LZ1 is still largest among the RMF calculations.

The PKO1, PKO2, PKO3, PKO1*, and PKA1 basically starts from the same Lagrangian, while considered mesons and their meson-nucleon couplings constant are different. The mesons considered in these EDFs are summarized in Table 3. This suggests that π -PV, ρ -T, and ρ -VT couplings, which gives the tensor interaction, are important to reproduce the kink behaviour. According to Ref. [31], the strength of the tensor interaction of PKO2 is weakest and that of PKO1* is the strongest; that of PKO3 is the second strongest, and those of PKA1 and PKO1 are marginal. Strengths of tensor interaction of these interactions are consistent with the kink size. Therefore, the tensor interaction or its outcomes, such as spin-orbit mean field and shell structure, is important to reproduce the kink behaviour. This is in contrast to the non-relativistic case.

The DD-LZ1 EDF is constructed guided by pseudo-spin symmetry [40] and, as a result, shell evolution was described better than other popular RMF EDFs [28]. It is constructed without ansatz of density dependences of some couplings and fitted to ^{218}U , which is related to the sub-shell closure of $Z = 92$. The pseudo-spin symmetry is strongly related to the spin-orbit splitting [41]. This fact is in agreement with our conjecture that the spin-orbit splitting is important to reproduce the kink size.

3.2. Single-Particle Energies

To understand these behaviours, the single-particle spectra of neutrons of ^{132}Sn are shown in Figs. 3 and 4. The magenta dotted line represents the $N = 82$ shell gap. All the calculations show that the $2f_{7/2}$ orbital is just above the $N = 82$

shell gap, but above the $2f_{7/2}$ orbital, the ordering of valence-neutron orbitals noticeably depends on the EDF utilized. Especially, the $1h_{9/2}$ orbital appears just above the $2f_{7/2}$ orbital in SAMi, SAMi-noT, SAMi-T, DD-PC1, PKO3, and PKO1* calculations, in which the kink is noticeably strong as listed in Tables 1 and 2. Therefore, the order of the single-particle orbitals above the shell gap may play an important role as mentioned in Ref. [7]. To understand the mechanism more deeply, the occupation probabilities of the single-particle orbitals just above the shell gap of ^{134}Sn are plotted in Figs. 5 and 6. The correlation between the occupation probability of $1h_{9/2}$ orbital and the slope above $N = 82$ gap ($\Delta R_{\text{ch}}^{\text{Sn}}(134)$) is plotted in Fig. 7. It is easily seen that, in general, the larger occupancy of the $1h_{9/2}$ orbital gives the steeper slope, and accordingly the larger kink, for instance, in SAMi, SAMi-noT, SAMi-T, and the PKO series. One phenomenological explanation on this kink-promoting effect of $1h_{9/2}$ is that, with the effective centrifugal potential for $l = 5$, the radial distribution of this single-particle orbital can be extended. Thus, when the two valence neutrons above the $N = 82$ shell are allowed to occupy this orbital, the mean radial distribution is suddenly enhanced. The DD-LZ1 again shows an exceptional behaviour: Its kink size is noticeably strong, although the occupation probability of the $1h_{9/2}$ orbital is small.

It is also shown that the occupation probability of $3p_{3/2}$ orbitals is much larger than $1h_{9/2}$ orbitals in the UNEDF0, UNEDF1, and UNEDF2, which show the ‘‘anti kink’’ behaviour at $N = 82$, while these anti kinks also originates from the steep slope below $N = 82$ and the slopes above $N = 82$ are only a little smaller than other Skyrme results.

By summarizing the above discussions, to reproduce the kink behaviour of R_{ch} at $N = 82$, the occupation probability of the $1h_{9/2}$ orbital, which locate above the $2f_{7/2}$ orbital, must be large enough. In order to lower the $1h_{9/2}$ orbital, the spin-orbit interaction should not be too strong; otherwise, the $1h_{9/2}$ energy becomes larger than the $2f_{7/2}$ one and the $3p_{3/2}$ energy can be too low, which is the origin of the anti kink. The spin-orbit gaps of the $1h$ orbitals calculated by the UNEDF0, UNEDF1, and UNEDF2 are almost the same as the other Skyrme EDFs except SAMi series; however, the occupation probabilities of $1h_{9/2}$ in the UNEDF0, UNEDF1, and UNEDF2 are smaller. This may be because the effective mass of the UNEDF series is one, while those of the other Skyrme EDFs are less than one; accordingly, the spin-orbit splitting of the UNEDF series becomes *effectively* large. Even though the strengths of isoscalar and isovector spin-orbit interactions, W_0 and W'_0 , are the same, the kink can appear; thus, the effect of W_0 and W'_0 to the kink behaviour is puzzling. The Skyrme tensor interaction also introduces the spin-orbit mean field, but its effect is tiny.

It should be noted that these two orbitals, $2f_{7/2}$ and $1h_{9/2}$, are pseudo-spin doublet; thus if the pseudo-spin symmetry exactly holds, these two orbitals completely degenerates, which may make the occupation probability of $1h_{9/2}$ larger. It is known that the relativistic calculation describes the pseudo-spin better; this may be another reason why the relativistic calculation describes the kink behaviour better. However, the better description of the pseudo-spin symmetry does not mean the pseudo-spin doublet are degenerated well; indeed, the DD-LZ1, which is expected

to give better description of the pseudo-spin symmetry, does not give such degeneration.

3.3. Parameters of Nuclear Equation of State

At last, it is discussed whether parameters of the equation of state (EoS) affect the kink behaviour. The SAMi EDF has three families: SAMi-J, SAMi-m, and SAMi-K families. In these families, the fitting criteria of the EDF parameters are basically the same as the SAMi EDF, while one of the EoS parameter is assumed to be different: SAMi-J assumes the different symmetry energy at the saturation density J , SAMi-m assumes the different effective mass m^* , and SAMi-K assumes the different incompressibility K_∞ . Figures 8, 9, and 10, respectively, show the slope $\Delta R_{\text{ch}}^{\text{Sn}}$ as functions of the mass number A for the SAMi-J, SAMi-m, and SAMi-K families. The results of the SAMi-K family show almost completely overlapped with each other; therefore, it can be concluded that the incompressibility K_∞ does not affect R_{ch} . Different SAMi-m EDF gives similar R_{ch} above the $N = 82$ gap but slightly different tendency at $66 \leq N \leq 82$. This may be because the effective mass changes the space of single-particle energies, which leads to the different occupancy, while the kink behaviour is almost the same.

Different SAMi-J EDF gives slightly different behaviour of R_{ch} above the $N = 82$ gap. For simplicity, let us assume that all the SAMi-J EDF gives the same R_{ch} at $N = 82$. Then, larger symmetry energy gives larger neutron radius of ^{132}Sn . Adding two neutrons to ^{132}Sn , these two neutrons changes the proton radius. The larger neutron radius leads to the larger proton radius of ^{134}Sn . Thus, the larger J gives the larger R_{ch} at $N > 82$.

3.4. Ca and Pb Isotopes

In the supplemental materials, results for Ca and Pb isotopes are shown. Results for Pb isotopes are basically the similar to those for Sn isotopes, while there are some difference, for instance, HFB9 and UNEDF2 give positive kinks, SGII and DD-PC1 gives significant kinks. Since properties of ^{208}Pb are frequently used for fitting criteria of EDFs, such differences appear. Results for Ca isotopes, especially, the $N = 28$ kink, are different from Sn isotopes, and systematic behaviours of R_{ch} , even $N < 28$, are not well described. Indeed, it is suggested in several works [7, 42, 43] that beyond-mean-field effects are non-negligible in Ca isotopes. The calculations presented in this paper do not include any beyond-mean-field effects. The fact that the kink behaviours of Ca isotopes are different from Sn and Pb isotopes implies that the mechanism of the behaviour of R_{ch} of Ca isotopes is different from the other isochains.

4. Conclusion

In this paper, the sudden change of the mass-number dependence of the charge radius at the neutron shell gap, so-called the kink behaviour, is discussed by using the non-relativistic Skyrme, relativistic mean field (RMF), and the relativistic Hartree-Fock (RHF) calculations. In general, the RHF calculation gives the larger kink and the Skyrme calculation gives the

smaller one, while the SAMi series gives exceptionally larger kink, and some Skyrme EDFs, for instance, UNEDF series, gives even the opposite behaviour. In order to reproduce the kink behaviour for the Sn isotopes, the occupation probability of the $1h_{9/2}$ orbital should be large enough. If the occupation probability of the $3p_{3/2}$ orbital is large, the anti kink may appear. In the case of Pb isotopes, larger occupation probability of the $1i_{11/2}$ orbital gives larger kink behaviour at the $N = 126$ gap. To make such occupancy, the spin-orbit mean-field must not be too strong.

Analyzing the RHF calculation, the tensor interaction, which leads to the spin-orbit mean-field potential, is concluded as essential to reproduce such occupation and the kink behaviour, while the effect of the Skyrme tensor interaction is tiny. The strengths of the isoscalar and isovector spin-orbit interactions in the Skyrme EDF, W_0 and W'_0 , may not be relevant to the kink behaviour, since the kink can appear even in $W_0 = W'_0$ case, as well as $W'_0 < 0 < W_0$ and $0 < W'_0 < W_0$ cases.

We also investigated whether parameters of nuclear equation of state affect such behaviour. It is found that neither the nuclear incompressibility nor the effective mass affects the kink behaviour, while the symmetry energy finitely affect it, whose mechanism is similar to the symmetry energy dependence of the neutron-skin thickness.

Mass number dependence of the charge radii of Ca isotopes is different from Sn or Pb isotopes, which implies the importance of beyond-mean-field effects in Ca isotopes.

Acknowledgment

The authors acknowledge for the fruitful discussion with Nobuo Hinohara, Tsunenori Inakura, Hitoshi Nakada, and Qiang Zhao. The authors also thank Xavier Roca-Maza for allowing us to use the SAMi-J, SAMi-K, and SAMi-m families. This work is partly supported by the RIKEN Special Postdoctoral Researcher Program, the Science and Technology Hub Collaborative Research Program from RIKEN Cluster for Science, Technology and Innovation Hub (RCSTI), the JSPS Grant-in-Aid for Scientific Research (C) under Grant No. 19K03858, and the JSPS Grant-in-Aid for Research Activity Start-up under Grant No. 22K20372. The numerical calculations were partly performed on cluster computers at the RIKEN iTHEMS program.

References

- [1] H. De Vries, C. W. De Jager, and C. De Vries, *At. Data Nucl. Data Tables* **36**, 495 (1987).
- [2] T. Suda and H. Simon, *Prog. Part. Nucl. Phys.* **96**, 1 (2017).
- [3] I. Angeli and K. P. Marinova, *At. Data Nucl. Data Tables* **99**, 69 (2013).
- [4] P. Campbell, I. D. Moore, and M. R. Pearson, *Prog. Part. Nucl. Phys.* **86**, 127 (2016).
- [5] P.-G. Reinhard and H. Flocard, *Nucl. Phys. A* **584**, 467 (1995).
- [6] H. Nakada, *Phys. Rev. C* **100**, 044310 (2019).
- [7] U. C. Perera, A. V. Afanasjev, and P. Ring, *Phys. Rev. C* **104**, 064313 (2021).
- [8] D. Vautherin and D. M. Brink, *Phys. Rev. C* **5**, 626 (1972).
- [9] L. D. Miller and A. E. S. Green, *Phys. Rev. C* **5**, 241 (1972).
- [10] J. D. Walecka, *Ann. Phys.* **83**, 491 (1974).

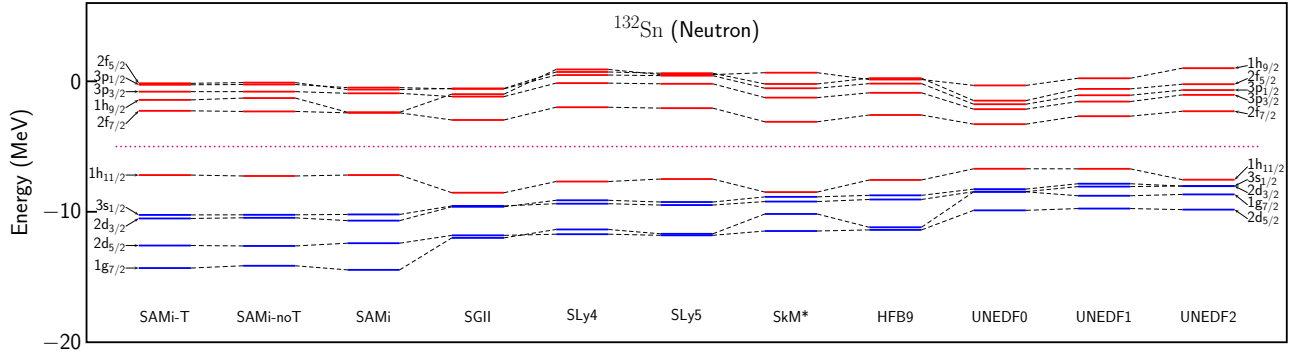


Figure 3: Single-particle spectra of ^{132}Sn calculated using the non-relativistic scheme.

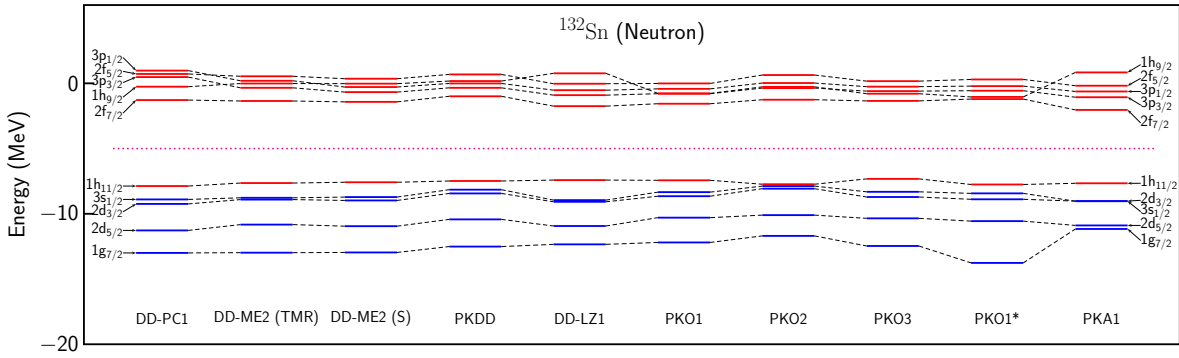


Figure 4: Same as Fig. 3 but using the relativistic scheme.

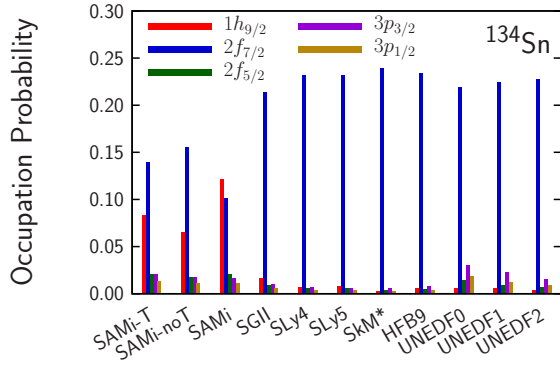


Figure 5: Occupation probability of orbitals above the $N = 82$ shell gap for ^{134}Sn calculated using the non-relativistic scheme.

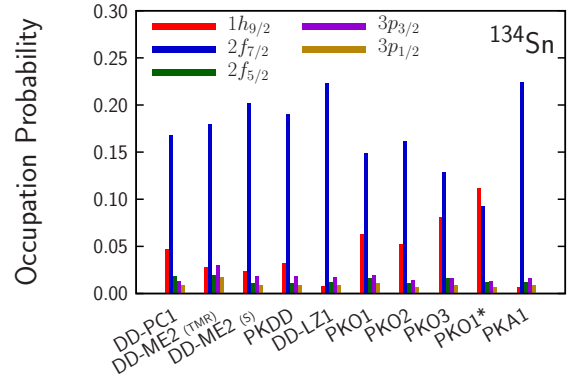


Figure 6: Same as Fig. 5 but using the relativistic scheme.

[11] W.-H. Long, N. Van Giai, and J. Meng, *Phys. Lett. B* **640**, 150 (2006).
 [12] X. Roca-Maza, G. Colò, and H. Sagawa, *Phys. Rev. C* **86**, 031306 (2012).
 [13] N. Van Giai and H. Sagawa, *Phys. Lett. B* **106**, 379 (1981).
 [14] E. Chabanat, P. Bonche, P. Haensel, J. Meyer, and R. Schaeffer, *Nucl. Phys. A* **635**, 231 (1998).
 [15] J. Bartel, P. Quentin, M. Brack, C. Guet, and H.-B. Håkansson, *Nucl. Phys. A* **386**, 79 (1982).
 [16] S. Goriely, M. Samyn, J. M. Pearson, and M. Onsi, *Nucl. Phys. A* **750**, 425 (2005).
 [17] M. Kortelainen, T. Lesinski, J. Moré, W. Nazarewicz, J. Sarich,

N. Schunck, M. V. Stoitsov, and S. Wild, *Phys. Rev. C* **82**, 024313 (2010).
 [18] M. Kortelainen, J. McDonnell, W. Nazarewicz, P.-G. Reinhard, J. Sarich, N. Schunck, M. V. Stoitsov, and S. M. Wild, *Phys. Rev. C* **85**, 024304 (2012).
 [19] M. Kortelainen, J. McDonnell, W. Nazarewicz, E. Olsen, P.-G. Reinhard, J. Sarich, N. Schunck, S. M. Wild, D. Davesne, J. Erler, *et al.*, *Phys. Rev. C* **89**, 054314 (2014).
 [20] S. Shen, G. Colò, and X. Roca-Maza, *Phys. Rev. C* **99**, 034322 (2019).
 [21] X. Roca-Maza, M. Brenna, B. K. Agrawal, P. F. Bortignon, G. Colò, L.-G. Cao, N. Paar, and D. Vretenar, *Phys. Rev. C* **87**, 034301 (2013).
 [22] X. Roca-Maza, Private communication.

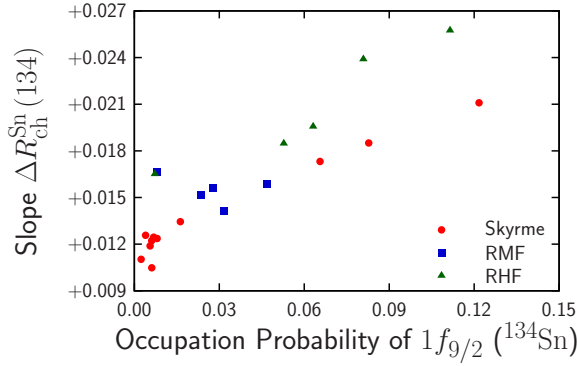


Figure 7: Correlation between occupation probability of $1f_{9/2}$ orbital of ^{134}Sn and kink size at $N = 82$.

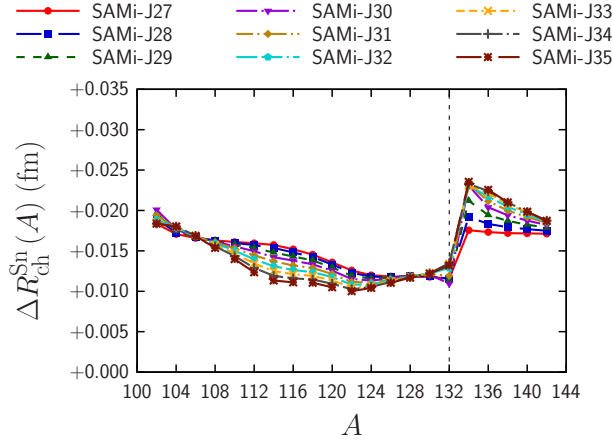


Figure 8: Same as Fig. 1(b) but by using the SAMi-J family.

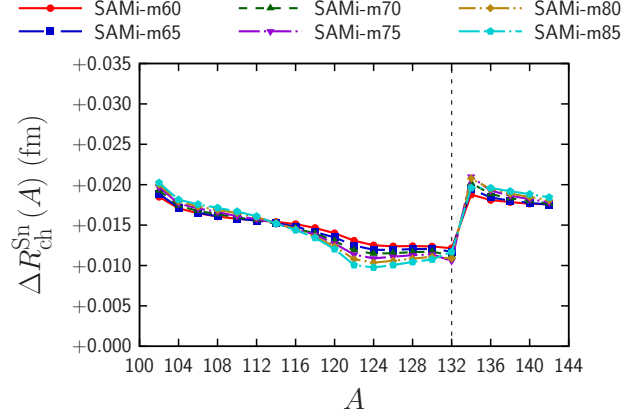


Figure 9: Same as Fig. 8 but by using the SAMi-m family.

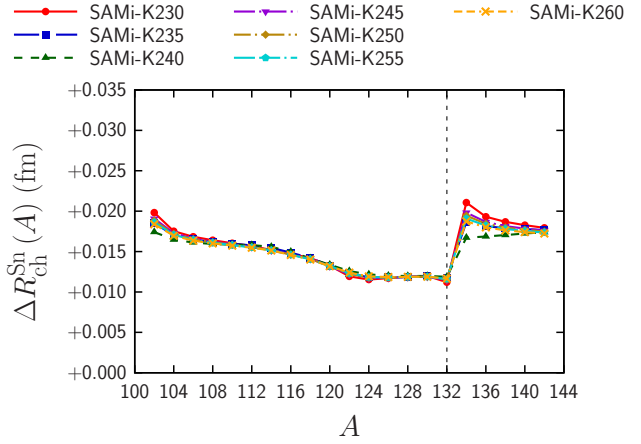


Figure 10: Same as Fig. 8 but by using the SAMi-K family.

- [23] J. Dobaczewski, H. Flocard, and J. Treiner, *Nucl. Phys. A* **422**, 103 (1984).
- [24] R. Navarro Perez, N. Schunck, R.-D. Lasserri, C. Zhang, and J. Sarich, *Comput. Phys. Commun.* **220**, 363 (2017).
- [25] T. Nikšić, D. Vretenar, and P. Ring, *Phys. Rev. C* **78**, 034318 (2008).
- [26] G. A. Lalazissis, T. Nikšić, D. Vretenar, and P. Ring, *Phys. Rev. C* **71**, 024312 (2005).
- [27] W. Long, J. Meng, N. Van Giai, and S.-G. Zhou, *Phys. Rev. C* **69**, 034319 (2004).
- [28] B. Wei, Q. Zhao, Z.-H. Wang, J. Geng, B.-Y. Sun, Y.-F. Niu, and W.-H. Long, *Chin. Phys. C* **44**, 074107 (2020).
- [29] W. H. Long, H. Sagawa, J. Meng, and N. Van Giai, *Europhys. Lett.* **82**, 12001 (2008).
- [30] W. Long, H. Sagawa, N. Van Giai, and J. Meng, *Phys. Rev. C* **76**, 034314 (2007).
- [31] Z. Wang, T. Naito, and H. Liang, *Phys. Rev. C* **103**, 064326 (2021).
- [32] Y. Tian, Z. Y. Ma, and P. Ring, *Phys. Lett. B* **676**, 44 (2009).
- [33] J. Dobaczewski, W. Nazarewicz, T. R. Werner, J. F. Berger, C. R. Chinn, and J. Dechargé, *Phys. Rev. C* **53**, 2809 (1996).
- [34] P. A. Zyla, R. M. Barnett, J. Beringer, O. Dahl, D. A. Dwyer, D. E. Groom, C.-J. Lin, K. S. Lugovsky, E. Pianori, D. J. Robinson, *et al.*, *Prog. Theor. Exp. Phys.* **2020**, 083C01 (2020).
- [35] T. Naito, G. Colò, H. Liang, and X. Roca-Maza, *Phys. Rev. C* **104**, 024316 (2021).
- [36] C. Gorges, L. V. Rodríguez, D. L. Balabanski, M. L. Bissell, K. Blaum, B. Cheal, R. F. Garcia Ruiz, G. Georgiev, W. Gins, H. Heylen, *et al.*, *Phys. Rev. Lett.* **122**, 192502 (2019).
- [37] S. A. Fayans, *JETP Lett.* **68**, 169 (1998).
- [38] S. V. Tolokonnikov, I. N. Borzov, M. Kortelainen, Y. S. Lutostansky, and E. E. Saperstein, *J. Phys. G* **42**, 075102 (2015).
- [39] P.-G. Reinhard and W. Nazarewicz, *Phys. Rev. C* **95**, 064328 (2017).
- [40] J. Geng, J. J. Li, W. H. Long, Y. F. Niu, and S. Y. Chang, *Phys. Rev. C* **100**, 051301 (2019).
- [41] H. Liang, J. Meng, and S.-G. Zhou, *Phys. Rep.* **570**, 1 (2015).
- [42] H. Sagawa, S. Yoshida, T. Naito, T. Uesaka, J. Zenihiro, J. Tanaka, and T. Suzuki, *Phys. Lett. B* **829**, 137072 (2022).
- [43] Z.-X. Yang, X.-H. Fan, T. Naito, Z.-M. Niu, Z.-P. Li, and H. Liang, Calibration of nuclear charge density distribution by back-propagation neural networks, arXiv:2205.15649 [nucl-th] (2022).

Supplemental Material of “Comparative Study on Charge Radii and Their Kinks at Magic Numbers”

Tomoya Naito^{a,b}, Tomohiro Oishi^c, Hiroyuki Sagawa^{d,e}, Zhiheng Wang^{f,g}

^aRIKEN Interdisciplinary Theoretical and Mathematical Sciences (iTHEMS), Wako, 351-0198, Japan

^bDepartment of Physics, Graduate School of Science, The University of Tokyo, Tokyo 113-0033, Japan

^cYukawa Institute for Theoretical Physics, Kyoto University, Kyoto 606-8502, Japan

^dCenter for Mathematics and Physics, University of Aizu, Aizu-Wakamatsu 965-8560, Japan

^eRIKEN Nishina Center, Wako 351-0198, Japan

^fSchool of Nuclear Science and Technology, Lanzhou University, Lanzhou 730000, China

^gFrontiers Science Center for Rare Isotopes, Lanzhou University, Lanzhou 730000, China

Abstract

In this supplemental material, the pairing strengths of the Skyrme interactions used in this paper and results for Ca and Pb isotopes are shown.

Appendix A. Pairing Strength

The pairing strengths of the Skyrme EDF used in this paper are summarized in Table A.1. The pairing interaction is the volume type

$$V_{\text{pair}}(\mathbf{r}_1, \mathbf{r}_2) = -V_0 \delta(\mathbf{r}_1 - \mathbf{r}_2) \quad (\text{A.1})$$

with the cutoff energy of 60 MeV.

Appendix B. Additional Information

In this section, the same results but for Ca and Pb isotopes are shown.

References

- [1] R. F. Garcia Ruiz, M. L. Bissell, K. Blaum, A. Ekström, N. Frömmgen, G. Hagen, M. Hammen, K. Hebeler, J. D. Holt, G. R. Jansen, *et al.*, *Nat. Phys.* **12**, 594 (2016).
- [2] A. J. Miller, K. Minamisono, A. Klose, D. Garand, C. Kujawa, J. D. Lantis, Y. Liu, B. Maaß, P. F. Mantica, W. Nazarewicz, *et al.*, *Nat. Phys.* **15**, 432 (2019).
- [3] I. Angeli and K. P. Marinova, *At. Data Nucl. Data Tables* **99**, 69 (2013).

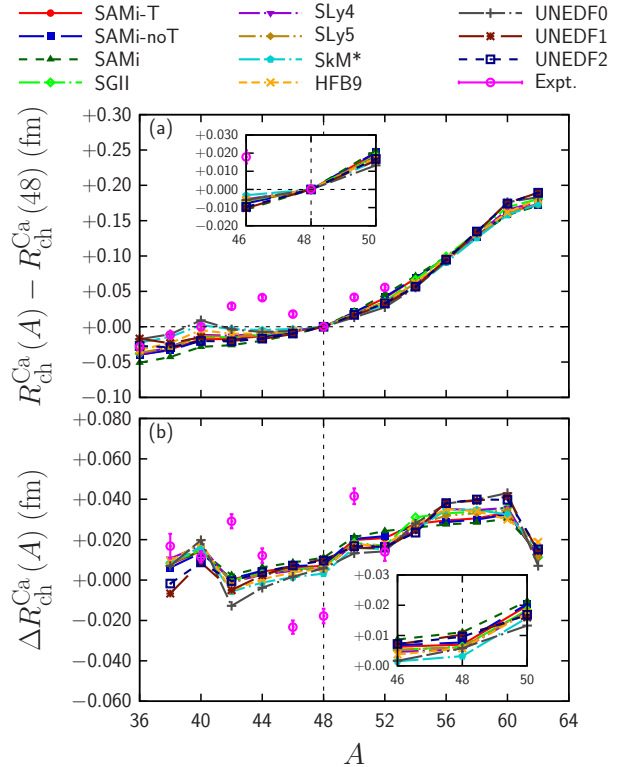


Figure B.1: Same as Fig. 1 but for Ca isotopes. Experimental data except ^{40}Ca are taken from Refs. [1, 2], instead of Ref. [3].

arXiv:2209.02857v1 [nucl-th] 6 Sep 2022

Table A.1: Pairing strengths for Skyrme EDFs used in this paper. The volume-type pairing interaction is used and the energy cutoff is 60 MeV.

Skyrme EDF	V_0 (MeV · fm ³)
SLy4	194.2
SLy5	188.2
HFB9	164.4
SkM*	156.2
SGII	169.8
UNEDF0	127.6
UNEDF1	138.4
UNEDF2	150.0
SAMi	213.7
SAMi-noT	216.4
SAMi-T	225.5
SAMi-K230	213.8
SAMi-K235	206.9
SAMi-K240	201.2
SAMi-K245	209.6
SAMi-K250	208.2
SAMi-K255	206.9
SAMi-K260	205.5
SAMi-m60	227.6
SAMi-m65	215.2
SAMi-m70	203.9
SAMi-m75	194.3
SAMi-m80	185.4
SAMi-m85	177.3
SAMi-J27	205.0
SAMi-J28	208.3
SAMi-J29	212.0
SAMi-J30	215.1
SAMi-J31	217.6
SAMi-J32	219.3
SAMi-J33	220.2
SAMi-J34	220.4
SAMi-J35	220.2

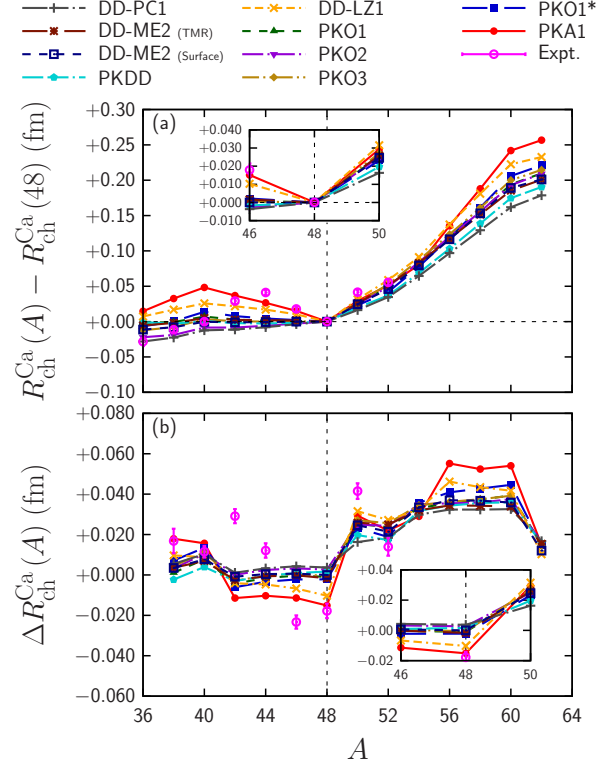


Figure B.2: Same as Fig. 2 but for Ca isotopes. Experimental data except ⁴⁰Ca are taken from Refs. [1, 2], instead of Ref. [3].

Table B.2: Same as Table 1 but of Ca together with $\Delta R_{\text{ch}}^{\text{Ca}}(48)$ and $\Delta R_{\text{ch}}^{\text{Ca}}(50)$.

EDF	$\Delta R_{\text{ch}}^{\text{Ca}}(48)$	$\Delta R_{\text{ch}}^{\text{Ca}}(50)$	$\Delta^2 R_{\text{ch}}^{\text{Ca}}$
UNEDF1	+0.010272	+0.015999	+0.003205
UNEDF2	+0.009611	+0.016829	+0.004745
UNEDF0	+0.005814	+0.013268	+0.005678
SAMi	+0.011096	+0.021330	+0.007340
SLy5	+0.006153	+0.018080	+0.008995
HFB9	+0.005729	+0.017407	+0.009052
SGII	+0.006334	+0.018378	+0.009252
SAMi-noT	+0.007689	+0.020381	+0.009451
SLy4	+0.005421	+0.017856	+0.009718
SAMi-T	+0.006976	+0.019841	+0.009773
SkM*	+0.003182	+0.015861	+0.010184
Expt.	-0.0482	+0.0697	+0.01179

Table B.3: Same as Table B.2 but by using relativistic EDF.

EDF	$\Delta R_{\text{ch}}^{\text{Ca}}(48)$	$\Delta R_{\text{ch}}^{\text{Ca}}(50)$	$\Delta^2 R_{\text{ch}}^{\text{Ca}}$
DD-PC1	+0.003671	+0.016293	+0.009053
PKDD	+0.001674	+0.019694	+0.014959
PKO2	+0.002670	+0.024965	+0.018927
DD-ME2 (Surface)	-0.000019	+0.024576	+0.021496
PKO1*	-0.002174	+0.023201	+0.022340
PKO1	-0.000956	+0.025284	+0.022742
DD-ME2 (TMR)	-0.001631	+0.025863	+0.023913
PKO3	-0.000550	+0.027110	+0.024125
DD-LZ1	-0.010279	+0.031533	+0.038630
PKA1	-0.015149	+0.029323	+0.041448
Expt.	-0.0482	+0.0697	+0.01179

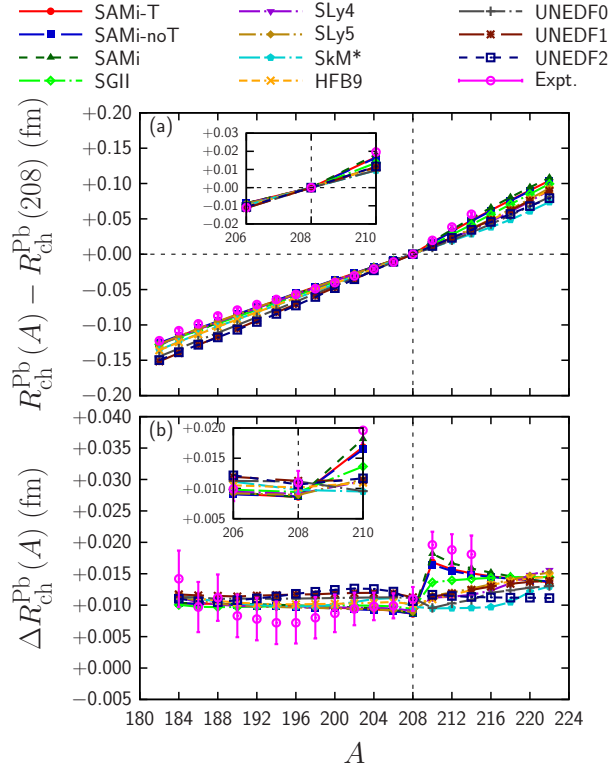


Figure B.3: Same as Fig. 1 but for Pb isotopes.

Table B.4: Same as Table 1 but of Pb together with $\Delta R_{\text{ch}}^{\text{Pb}}(208)$ and $\Delta R_{\text{ch}}^{\text{Pb}}(210)$.

EDF	$\Delta R_{\text{ch}}^{\text{Pb}}(208)$	$\Delta R_{\text{ch}}^{\text{Pb}}(210)$	$\Delta^2 R_{\text{ch}}^{\text{Pb}}$
UNEDF0	+0.011157	+0.009561	-0.001213
UNEDF1	+0.011244	+0.011363	+0.000721
SkM*	+0.009764	+0.009491	+0.000792
HFB9	+0.010160	+0.010945	+0.001504
UNEDF2	+0.010646	+0.011670	+0.001968
SLy4	+0.009096	+0.011210	+0.002690
SLy5	+0.008920	+0.011507	+0.002969
SGII	+0.009396	+0.013625	+0.004459
SAMi-noT	+0.008684	+0.016457	+0.006378
SAMi-T	+0.008595	+0.016829	+0.006602
SAMi	+0.008571	+0.018176	+0.007542
Expt.	+0.0110	+0.0196	+0.0086

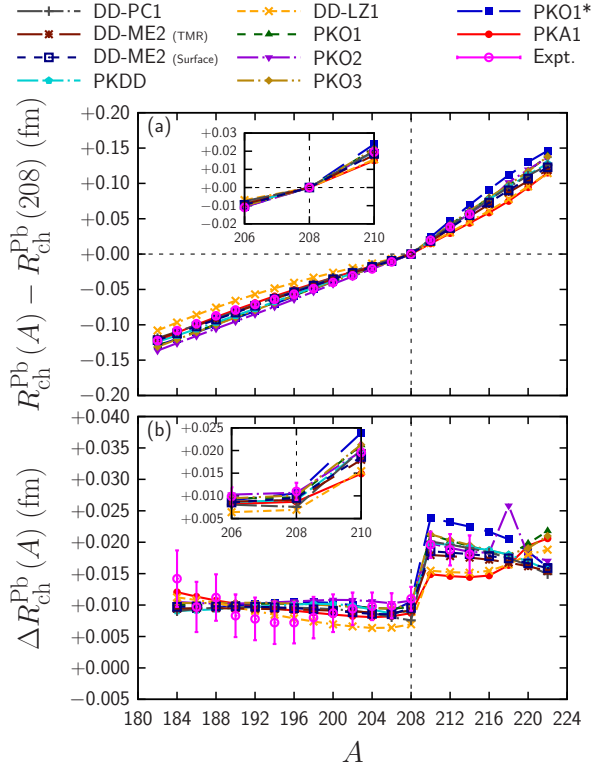


Figure B.4: Same as Fig. 2 but for Pb isotopes.

Table B.5: Same as Table B.4 but by using relativistic EDF.

EDF	$\Delta R_{\text{ch}}^{\text{Pb}}(208)$	$\Delta R_{\text{ch}}^{\text{Pb}}(210)$	$\Delta^2 R_{\text{ch}}^{\text{Pb}}$
PKA1	+0.008709	+0.014888	+0.006571
DD-ME2 (TMR)	+0.009133	+0.017962	+0.008379
DD-ME2 (Surface)	+0.009537	+0.018567	+0.008535
DD-LZ1	+0.006935	+0.015462	+0.008626
PKO2	+0.010694	+0.019800	+0.008717
PKO3	+0.010103	+0.021265	+0.010230
PKDD	+0.009105	+0.019879	+0.010233
PKO1	+0.009690	+0.021183	+0.010711
DD-PC1	+0.007566	+0.020118	+0.011839
PKO1*	+0.010553	+0.023893	+0.012488
Expt.	+0.0110	+0.0196	+0.0086

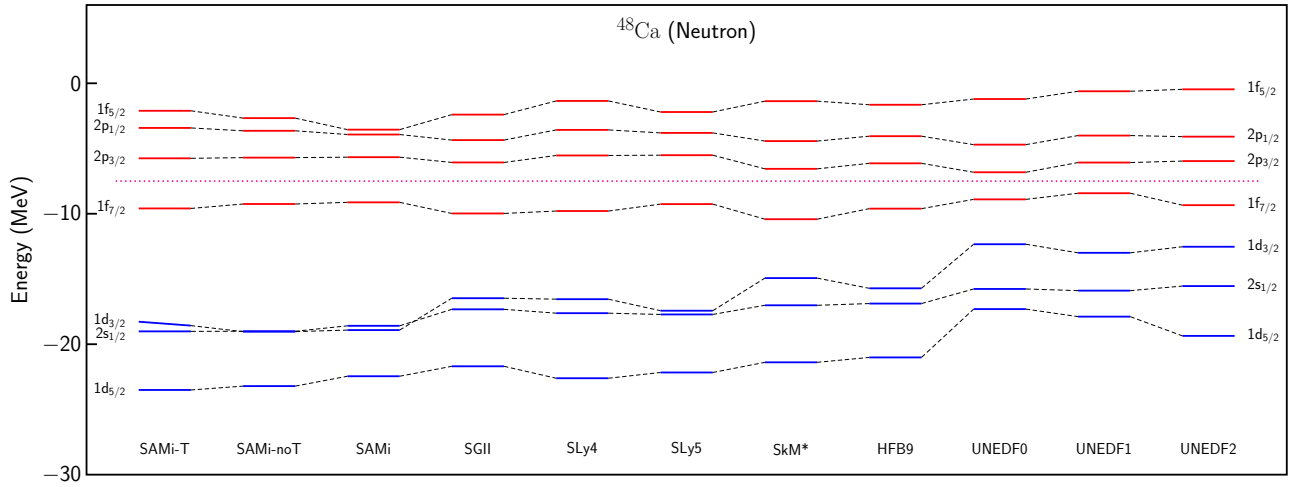


Figure B.5: Same as Fig. 3 but of ^{48}Ca .

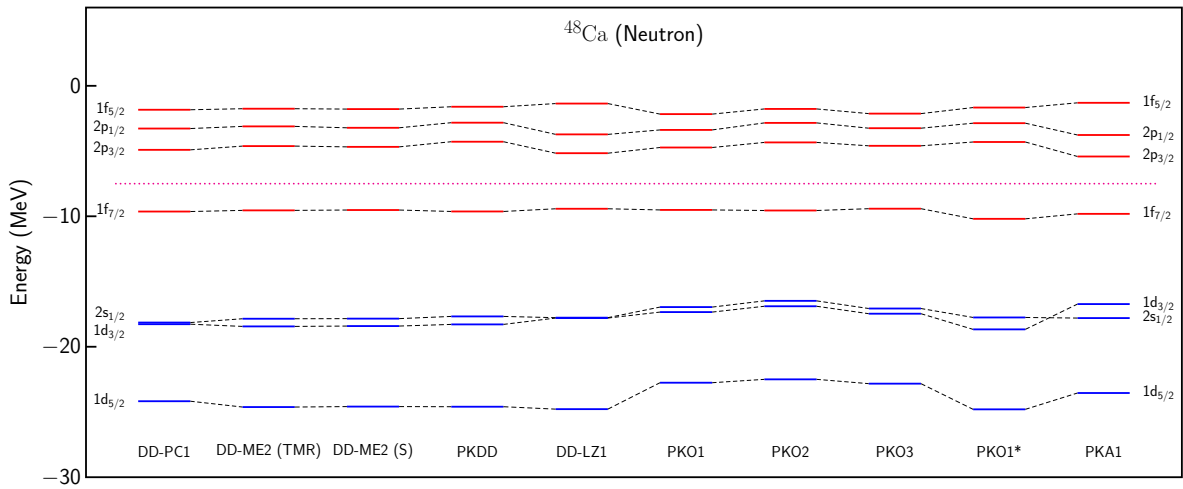


Figure B.6: Same as Fig. B.5 but using the relativistic scheme.

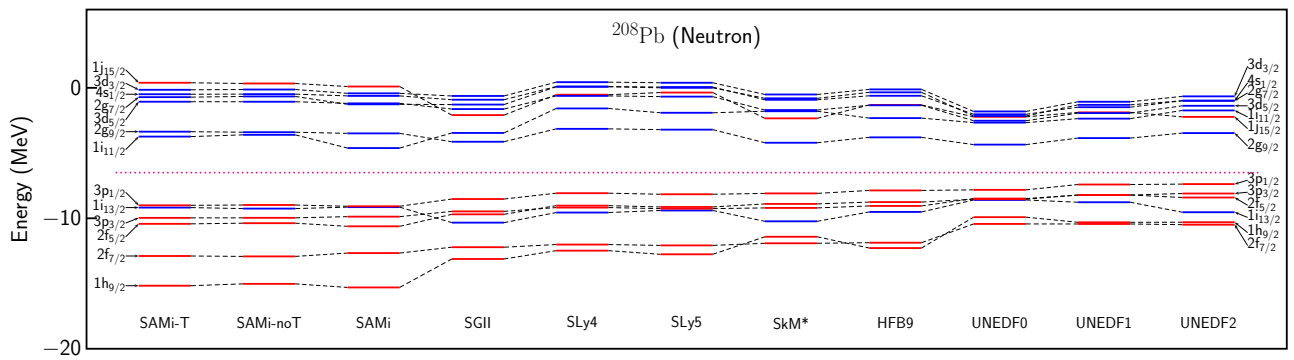


Figure B.7: Same as Fig. 3 but of ^{208}Pb .

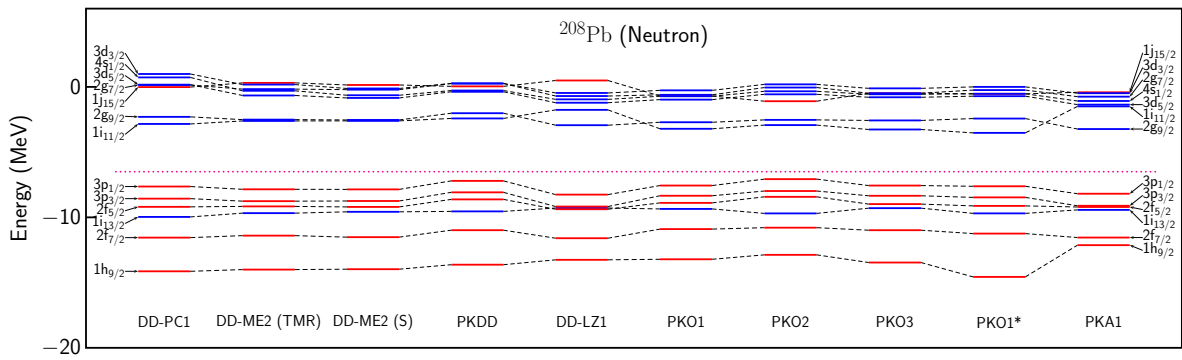


Figure B.8: Same as Fig. B.7 but using the relativistic scheme.

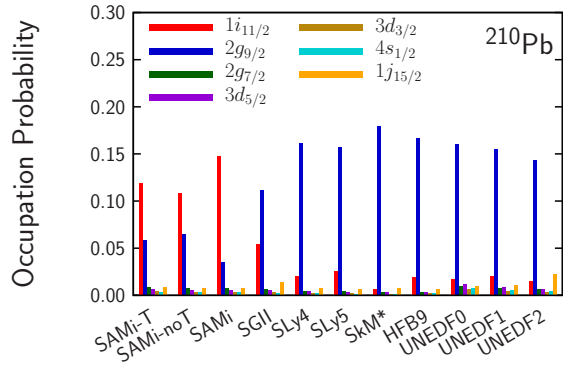


Figure B.9: Occupation probability of orbitals above the $N = 126$ shell gap for ^{210}Pb calculated using the non-relativistic scheme.

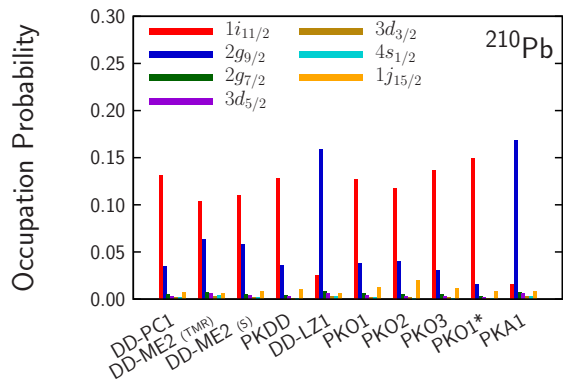


Figure B.10: Same as Fig. B.9 but using the relativistic scheme.

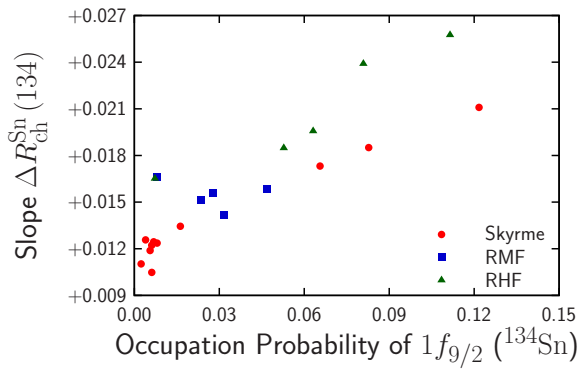


Figure B.11: Correlation between occupation probability of $1i_{11/2}$ orbital of ^{210}Pb and kink size at $N = 126$.